



## Deformation behavior of a NiCo multilayer with a modulated grain size distribution



Matthew Daly<sup>a</sup>, Jonathan Lawrence McCrea<sup>b</sup>, Brandon Andrew Bouwhuis<sup>b</sup>,  
Chandra Veer Singh<sup>a</sup>, Glenn David Hibbard<sup>a,\*</sup>

<sup>a</sup> Department of Materials Science and Engineering, University of Toronto, 184 College Street, Suite 140, Toronto, Ontario, Canada M5S 3E4

<sup>b</sup> Integran Technologies Inc., 6300 Northam Drive, Mississauga, Ontario, Canada L4V 1H7

### ARTICLE INFO

#### Article history:

Received 15 April 2015

Received in revised form

16 June 2015

Accepted 16 June 2015

Available online 20 June 2015

#### Keywords:

Cellular materials

Nanostructured materials

Plasticity

Fracture

Mechanical characterization

### ABSTRACT

In order to gain a fundamental understanding of the deformation behavior of multilayer architectures composed of a periodic layering of hard and soft structural features, NiCo samples possessing modulated nanocrystalline and coarse-grained microstructures were fabricated using pulsed electrodeposition. Scanning electron microscopy imaging confirmed that the samples possessed an alternating grain size distribution and the desired 1:1 thickness ratio of constitutive layers. Uniaxial tensile testing showed a rule of mixtures relationship in yield and ultimate tensile strengths for the multilayer with respect to reference samples. Notably, an increase in elongation to failure was observed in the multilayer when compared to the nanocrystalline reference. The gains in elongation were found to be associated with improved neck stability due to dislocation activity within the coarse-grained layers. The morphology of the fracture surface, considered together with the available mechanical data, electron micrographs and texture measurements, forms the basis of a multiscale deformation mechanism which describes a failure pathway for multilayer architectures with nanocrystalline and coarse-grained structural features.

© 2015 Elsevier B.V. All rights reserved.

### 1. Introduction

Multilayers (ML)s are a layering of alternating material structures and represent an architecture which may be engineered to improve the relative mechanical properties of the constituent material components [1–4]. In traditional ML architectures, immiscible metallic species are selected for layering such that geometric confinement imposed by layer interfaces is augmented by lattice misfit between constituents, leading to increases in interfacial barrier strength [5,6]. The layer thicknesses may also be controlled in order to encourage specific dislocation-based strengthening mechanisms. For example, experimental and atomistic simulations have shown that as layer thicknesses reach into the nanometer regime, interfacial confinement effects suppress traditional Hall–Petch hardening and dislocation pile-up phenomena [7–9]. At these length scales, conventional dislocation-based plasticity is supplanted by dislocation confinement and transmission within individual layers, leading to significant gains in mechanical strength that exceed Hall–Petch predictions [7–9]. Once layer thicknesses approach sizes comparable to a dislocation core (~1–2 nm), interfacial barrier strength has been shown to

reduce, promoting interlayer dislocation transmission and, consequently, a reversal of strength improvements from geometric scaling effects [10].

Although the presence of nanoscale geometric features in metallic MLs has led to impressive improvements in strength, as discussed by Anderson et al. [2], confinement from a high density of interfacial misfit dislocations may lead to notable decreases in ductility and a ductile–brittle transition in fracture behavior. For example, uniaxial tensile tests of Cu/Ag MLs show a two-fold decrease in elongation to failure at layer thicknesses of less than 40 nm, when compared against monolithic samples of the same materials [11]. A similar finding was echoed in a tensile investigation of Cr/Cu MLs [12], where the dislocation storing capability of the relatively ductile Cu constituent becomes compromised at layer thicknesses less than 100 nm. In nanoscale Cu/Au and Cr/Cu MLs, these reductions in elongation to failure manifest macroscopically as fracture surfaces exhibiting brittle failure [13]. Ultimately, lattice mismatch at interfacial structures in traditional MLs are generally detrimental to plastic flow, making preservation of the intrinsic ductility of such material architectures problematic. Additionally, in the case of hard-soft nanostructured MLs such as Cr/Cu, material elongation is further handicapped by a significant decrease in the dislocation storage capability of the Cu layer at nanometer thicknesses [13]. In a notable exception to this property trend, Mara et al. [14] have reported a measurement of ultra-high strength and a ductility of greater than

\* Corresponding author.

E-mail address: [glenn.hibbard@utoronto.ca](mailto:glenn.hibbard@utoronto.ca) (G.D. Hibbard).

0.25 true strain in 5 nm Cu/Nb ML pillars under compressive loading. It is unclear from this study, however, if similar strains may be achieved under tensile loading. From a mechanics perspective, the direction of loading relative to the ML stacking direction is also an important consideration. In this work, the referenced literature refers to loadings directed perpendicular to the layering direction in the ML.

The effect of interfaces on strengthening and elongation to failure in MLs may be considered in the greater realm of nanostructured materials. Despite impressive Hall–Petch strengthening properties [15,16], bulk nanocrystalline metals have also typically suffered from reduced ductility relative to their polycrystalline analogs due to early plastic instability during tensile loading [17,18]. Recently, monolithic alloys possessing hybrid microstructures composed of a bimodal distribution of nanocrystalline (NC) and coarse-grained (CG) crystals have been suggested as material architectures possessing both high strength and good ductility [19–22]. This concept of a bimodal grain size distribution may be adopted into the ML architecture, permitting a modulated microstructure with a low interfacial threshold to dislocation mobility. In comparison to traditional MLs, a NC–CG architecture is expected to significantly reduce interfacial lattice misfit and encourage dislocation activity between constituent layers, thereby providing an avenue for assessment of deformation evolution in modulated microstructures. A recent study from Kurmanava et al. [23] examined the mechanical properties of a NiFe ML. Compared to a NC reference, however, the ductility of the ML was reported to be in fact slightly reduced. This surprising finding was found to be caused by the combination of FCC and BCC phases in the sample microstructures [23], further implicating the influence of lattice misfit on sample ductility. This result underscores the need for a monophase material, from which the impact of grain fidelity modulation and implementation of the ML architecture may be directly assessed.

In an effort to understand the intrinsic deformation behavior of ML structures comprised of hard and soft features, the current study investigates the mechanical properties of a Ni<sub>80</sub>Co (wt%) ML with an alternating grain size distribution. The NiCo system was selected for study as the metallic species exhibit solid solubility in a FCC unit cell for material chemistries greater than 40 wt% Ni [24] and NC NiCo is known to possess enhanced thermal stability [25]. The purpose of this study is two-fold: firstly, improvements in material plasticity achieved from a combination of NC and CG microstructures are examined; secondly, the unique architecture of the NiCo ML offers the opportunity to study the deformation behavior of relatively soft coarse-grained microstructures confined by hard nanocrystalline structural features. Due to its monolithic construction, deformation may proceed in the hard–soft ML without inhibition to dislocation activity from interfacial lattice misfit. In an effort to rigorously assess the deformation behavior of the ML architecture, microscale architectural features and plasticity must be considered. Therefore the current study investigates both micro and macroscale deformation events in order to provide a comprehensive multiscale characterization of the mechanical response of MLs with modulated microstructures.

## 2. Methods and materials

Free-standing NiCo plates were fabricated at Integran Technologies Inc. using pulsed electrodeposition (PED) on an inert stainless steel cathode from a proprietary electroplating solution and process. This procedure is known to create high quality samples and the PED process is described in greater detail in [26–28]. CG and NC layers were deposited by modifying the cathodic pulse shape to achieve the desired microstructure. The PED parameters were varied to create a ML with a 1:1 CG–NC thickness

ratio. Bulk CG and NC sheets were also fabricated to serve as a comparative reference for mechanical testing. Bath chemistries were maintained to produce a nominal Ni<sub>80</sub>Co (wt%) alloy composition. Following PED, the sheets were mechanically stripped from the stainless steel cathode. Tensile coupons with a 100 mm length, 10 mm grip width, 3.5 mm grip fillet radius, and a nominal gauge dimension measuring 33 mm long ( $L_0$ ) by 3 mm wide ( $W_0$ ) were cut from the bulk sheets using a waterjet. The resulting coupons were deburred and ground to at least a grit of 600 with SiC abrasive papers to remove any obvious surface flaws from the gauge length. The coupons all possessed thicknesses ( $t_0$ ) ranging from 0.5 to 0.7 mm. A small taper was present in the tensile coupon cross-sections due to the waterjetting process, creating a slightly trapezoidal gauge area. All measurements reported in this study use the caliper dimension for calculation where applicable. Deviations in nominal measurements due to tapering of the gauge area are rather low and were measured to be in the range of 3–5% for the specimens examined in this study. It should be noted that the effects of this measurement error did not alter the statistical significance of the presented data.

The as-deposited microstructure of the NiCo ML was imaged using scanning electron microscopy (SEM) and PED alloy chemistries were confirmed with energy dispersive X-ray (EDX) analysis using a Hitachi SU 3500 instrument. For SEM imaging, samples were progressively ground to a grit of 1200 and then polished using 50 nm colloidal silica suspension. Vibratory polishing in colloidal silica suspension was then performed for 4 h as the final polishing step. Colloidal silica residue was removed through Ar ion milling at a 6 kV accelerating voltage with a gracing angle of 8° for 10 min. At low magnification (Fig. 1a), it can be seen that the NC and CG layers appeared to have a near equal thickness throughout the full sample cross-section. The orientation of the tensile coupon dimensions relative to the features of the ML are indicated in the figure. At higher magnifications (Fig. 1b and c), a clear interface between NC and CG layers was observed, and the elongated morphology of the CG microstructure became evident. Based on the collected micrographs, the CG and NC layers were measured to be in the range of 5–10  $\mu$ m thick. An asymmetric grain morphology associated with the PED growth direction (image down) of the CG layer was visible at high magnification (Fig. 1c). The facets of the terminal structures created a characteristic roughness in the ML interface on the order of 1–2  $\mu$ m, which has been previously observed in Fe MLs [29]. EDX analysis confirmed that the PED sample chemistries were near target, with Co compositions of 19, 17, and 20 wt% measured for the CG, ML, and NC samples, respectively. Note that previous studies of NiCo manufactured by a similar PED procedure report sulphur and carbon concentrations on the order of several hundred ppm [25].

The texture and the grain size of the CG layers were characterized using electron backscatter diffraction (EBSD) mapping. EBSD maps were collected with a step size of 300 nm and an indexing of over 85% was achieved. Due to the high number of interfaces in the PED samples, a conservative interpolation algorithm was utilized to smoothen EBSD results, which had a negligible impact on the orientation distribution of the collected measurements. According to the collected EBSD maps (Fig. 2), the morphology of the CG layers was columnar, with major and minor grain axis measurements in the range of approximately 5–8 and 3–5  $\mu$ m, respectively. For EBSD analysis, grain boundaries were defined as adjacent regions with a greater than 10° misorientation. Fig. 2a and b presents the sample texture in the  $t_0$  (growth orientation) and  $L_0$  directions and the corresponding orientation distribution functions of the collected EBSD data is provided in Fig. 2c and d, respectively. According to the EBSD texture data, the CG layer possess a strong  $\langle 100 \rangle$  fiber texture along the growth orientation (Fig. 2c), which is common in PED materials [30] and was reported in NiFe MLs [23]. Given this orientation restriction, the EBSD pole figures along the loading axis ( $L_0$ )

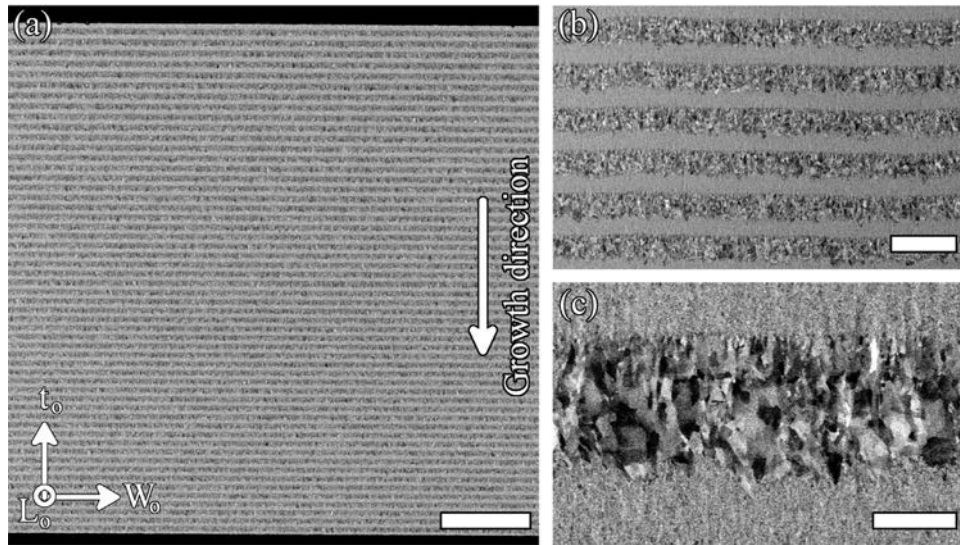


**Fig. 1.** Low (a), intermediate (b) and high (c) magnification micrographs of the as-deposited ML revealed through backscatter SEM imaging. The ML lacked any observable porosity, and possessed a periodic spacing and 1:1 thickness ratio of NC and CG layers. The orientation of tensile coupon dimensions relative to the SEM image is indicated in (a). The scale bars represent lengths of 100 (a), 20 (b) and 5  $\mu\text{m}$  (c). The growth direction of the ML from PED is indicated in (a).

show a preferred  $\langle 0kl \rangle$  orientation (Fig. 2d).

The grain size of the NC structure was characterized using X-ray diffraction (XRD) peak broadening analysis with a Rigaku MiniFlex 600 Benchtop instrument under  $\text{Cu-K}\alpha$  radiation ( $\lambda = 0.154 \text{ nm}$ ). In order to sample the cross-sectional dimension of the NC layer, the XRD spectra were collected to measure texture along the loading axis. According to XRD analysis (Fig. 3), the NC

reference sample possessed a texture with the  $(111)$  peak exhibiting the strongest diffraction condition and the  $(111)$   $(200)$  and  $(220)$  peaks had relative intensities of 100, 59 and 46, respectively. In comparison to a random texture (Ni powder), which possess relative peak intensities of 100, 42 and 21 for the first three peaks [31], the NC sample exhibited some texturing in the  $(200)$  and  $(220)$  directions. Using the Scherrer formula, an estimate of a

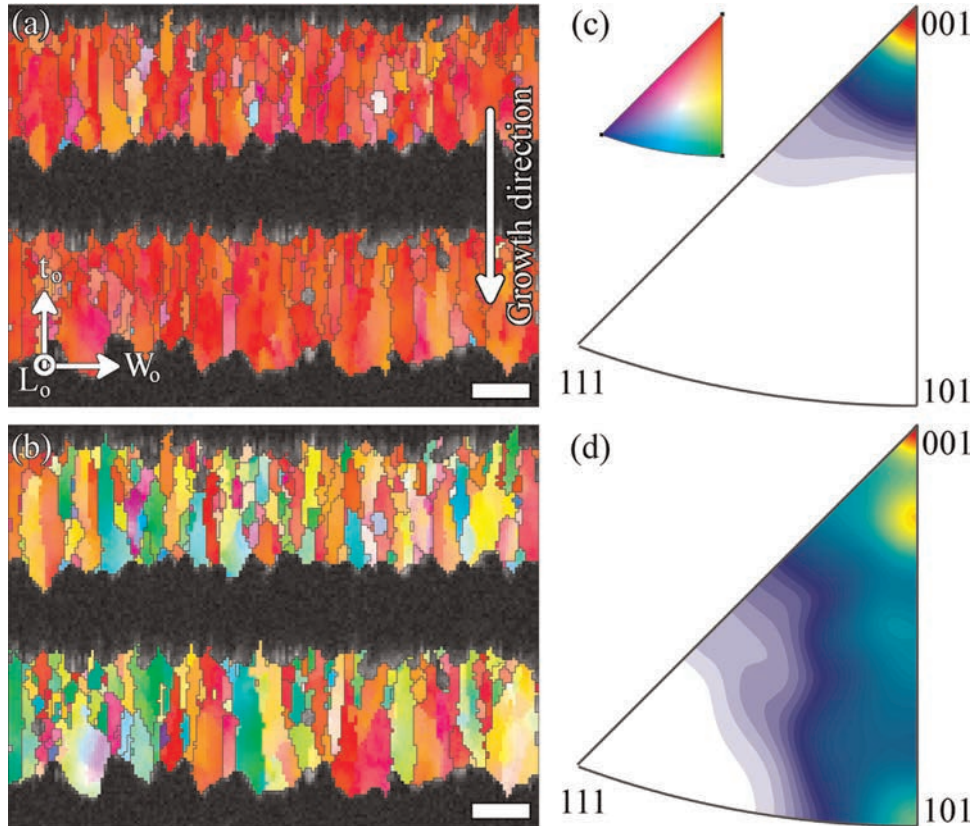


**Fig. 2.** EBSD maps collected showing the CG texture along the growth orientation (a) and loading axis (b), which fall along the  $t_0$  and  $L_0$  directions, respectively. The CG microstructure appeared to have a columnar morphology with many grains transcending the entire layer. (c and d) The respective orientation distribution functions calculated for the EBSD patterns in (a and b) indicated a strong  $\langle 100 \rangle$  fiber texture along the growth direction (a) and a  $\langle 0kl \rangle$  texture along the loading direction (b). The colormap in (c) corresponds to the inverse pole figure of the EBSD data in (a and b). The scale bars represent lengths of 5  $\mu\text{m}$ .

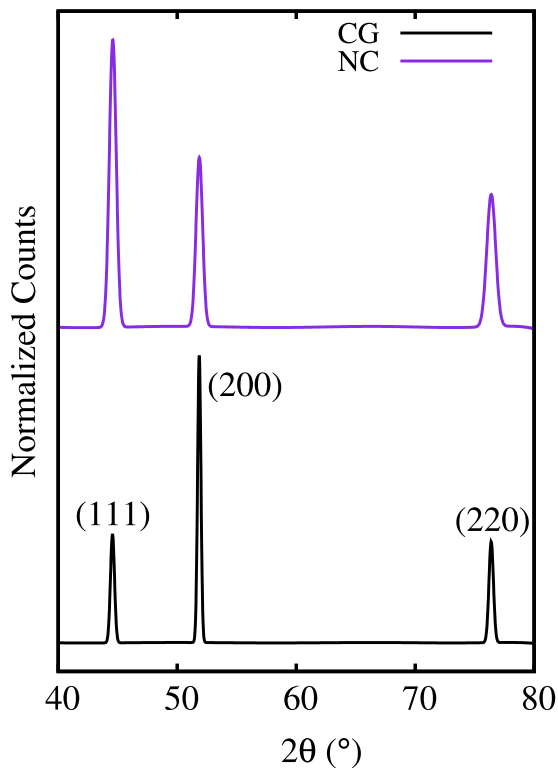


**Fig. 3.** XRD spectra of the NC and CG reference samples. In contrast to the strong (200) texture in the CG sample, a (111) dominated texture was observed in the NC reference. The XRD spectra refer to texture measurements along the loading axis.

17 nm average grain size for the NC microstructure was obtained after correction for instrument peak broadening. This grain size is typical for NiCo electrodeposits synthesized using comparable plating conditions [25]. Additionally, XRD analysis of the CG reference revealed a pronounced (200) peak, with relative intensities of 38, 100 and 35 for the (111) (200) and (220) peaks, respectively. These spectra are in good agreement with EBSD results in Fig. 2b for the CG layer in the ML. Secondary phases were not detected in the XRD spectra of the CG and NC PED samples, which is consistent with previous studies [25].

Room temperature ( $\sim 20^\circ\text{C}$ ) mechanical measurements were collected via uniaxial tensile testing at a cross-head velocity of 1 mm/min ( $5 \times 10^{-4}$ /s). In order to avoid errors associated with machine compliance, an extensometer with a 25.4 mm gauge was used. All tensile coupons were observed to fail within the extensometer gauge length. Additionally, digital image correlation (DIC) in combination with a camera system was utilized to provide local strain mapping during tensile necking. The camera system was configured to capture photographs at a frequency of 1 Hz, which corresponded to one photograph per  $5 \times 10^{-4}$  increment of engineering strain. Fractography of failed tensile coupons was performed using SEM imaging and trenching of the ML fracture surface to reveal NC and CG features was achieved with a focused ion beam (FIB) milling instrument under protective tungsten layer deposition.

### 3. Results and discussion

#### 3.1. Tensile properties and fractography of the PED samples

Fig. 4 presents the engineering stress–strain curves ( $\sigma$ ,  $\epsilon$ ) of representative CG, ML and NC samples. The yield ( $\sigma_{YS}$ ) and ultimate

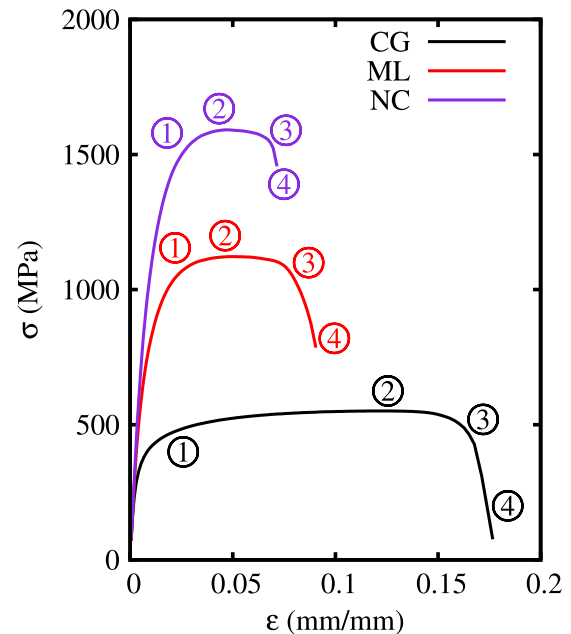


**Fig. 4.** Uniaxial tensile response of the PED samples. In terms of yield and ultimate strengths, the ML sample appeared to follow a rule of mixtures behavior. The elongation to failure of the ML sample was also higher with respect to the NC reference. Notably, non-uniform elongation appeared to be improved with respect to the NC specimen, which indicated a better developed and stable neck. The callouts on the stress–strain curve correspond to loading stages in the DIC analysis presented in Fig. 8.

tensile strengths ( $\sigma_{UTS}$ ) of the CG, ML and NC samples were measured to be  $365 \pm 48$ ,  $664 \pm 15$  and  $1017 \pm 30$  MPa and  $557 \pm 11$ ,  $1112 \pm 24$  and  $1622 \pm 39$  MPa, respectively.  $\sigma_{YS}$  was determined using the 0.2% strain offset definition and error is reported here as a 95% confidence interval ( $n=3$ ). In terms of elongation to failure, the CG and NC reference samples exhibited the expected elastic–plastic material responses, with evidence of necking occurring in both specimens. Due to the limited dislocation storage capacity of the NC microstructure, the ductility of the NC sample was substantially less than the CG reference. The post-yielding elongation of the PED samples may be divided into two categories, with elongation occurring prior to and after peak load  $\sigma_{UTS}$ , representing the uniform ( $\epsilon_u$ ) and non-uniform ( $\epsilon_{nu}$ ) deformation of the sample [32]. Based on this classification,  $\epsilon_u$  and  $\epsilon_{nu}$  values of  $0.113 \pm 0.007$  and  $0.049 \pm 0.009$  (CG),  $0.042 \pm 0.003$  and  $0.027 \pm 0.015$  (ML), and  $0.037 \pm 0.004$  and  $0.020 \pm 0.006$  (NC) were measured for the PED samples, respectively. As expected, the CG reference possessed the highest uniform elongation. Additionally, the ML sample possessed only marginally higher uniform elongation when compared against the NC reference, highlighting the role of the NC layer in the initiation of necking.

Although measurements indicated the ML sample possessed superior non-uniform deformation characteristics, when compared to the NC reference, it is difficult to draw strong conclusions from these values due to the inherently large error in end-of-life measurements of elongation. Therefore, planar images of fracture surfaces were collected and the reduction in area ratios ( $R_a$ ) for the tested specimens were compared.  $R_a$  is defined here as the ratio of original area before deformation to final fracture area, as projected onto the plane formed by  $W_0$  and  $t_0$ . Fig. 5 presents representative fracture surfaces of the PED samples. Comparatively, the CG sample exhibited the largest degree of necking, whereas the NC reference did not appear to have a significant neck. The ML sample showed an intermediary fracture behavior, with the development of a neck visible in the SEM image. Based on image analysis, the CG, ML and NC samples were found to have area reductions of

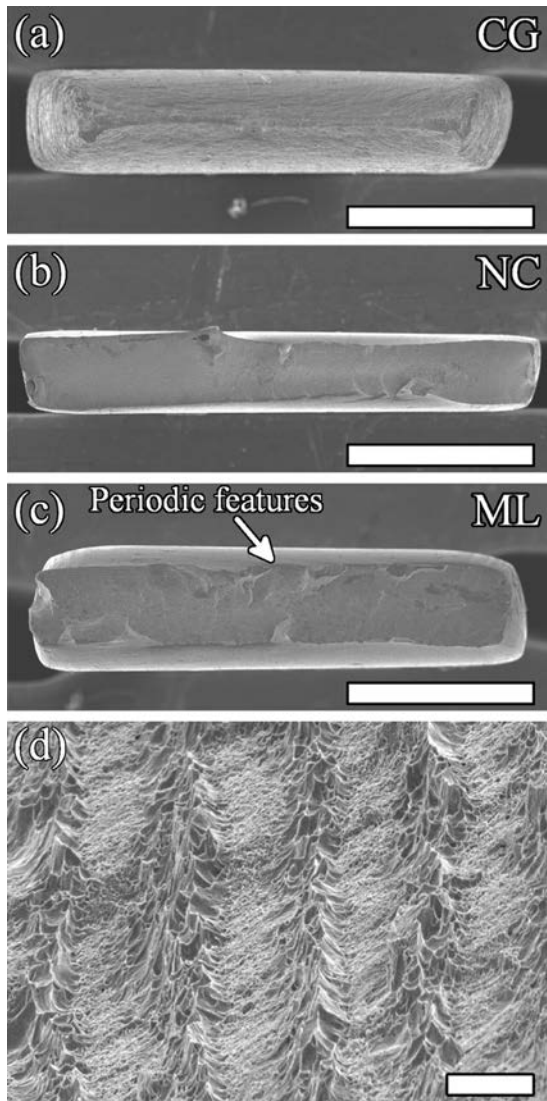


**Fig. 5.** SEM micrographs of the CG (a), NC (b), and ML (c) fracture surfaces which were captured from the perspective of the loading axis. (d) A high magnification SEM image of the periodic features observed in the ML fracture surface. The coarse and fine dimpled structures were formed by microvoid coalescence fracture modes in the CG and NC layers respectively. The scale bars are 1 mm in (a)–(c) and 5  $\mu\text{m}$  in (d).

$12.2 \pm 1.1$ ,  $2.0 \pm 0.2$  and  $1.5 \pm 0.2$ , respectively. From these calculations, the ML sample was found to possess a statistically significant ( $p < 0.05$ ) larger reduction ratio than the NC reference. Furthermore, the effects of cross-sectional dimensions on the ability of the coupon to form a well-developed neck cannot explain the relative increase in  $R_a$  for the ML sample [33]. On the other hand, the  $R_a$  of the ML structure was still considerably lower ( $\sim 6$  times) than the CG sample, which suggested that the fracture behavior of the ML was influenced significantly by the presence of the NC layer. Careful inspection of the ML fracture surface (Fig. 5c) revealed a periodic stacking of microscopic features which transcended the relief cross-section. A high magnification SEM image of the ML fracture surface (Fig. 5d) revealed a sequence of coarse and fine dimpled structures which corresponded to microvoid coalescence failure modes in the CG and NC layers respectively. A recent study of hard–soft Cr/Cu MLs has also reported similar microscopic features along the fracture surface, with the protrusions being identified as the ductile Cu layers [12].

A summary of the collected mechanical properties of the PED samples is provided in Fig. 6 and Table 1. The measured values of

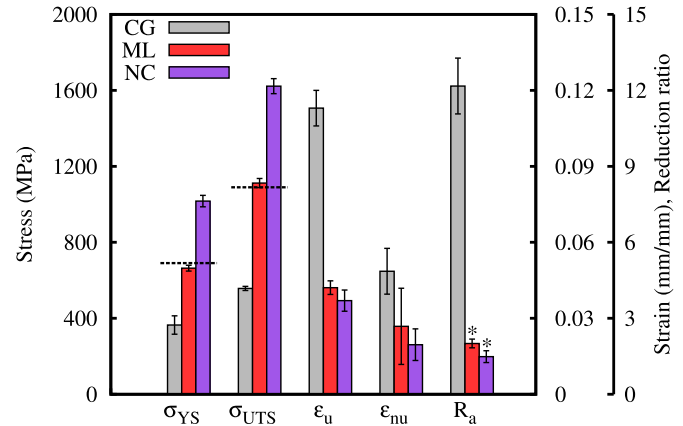


**Fig. 6.** A summary of the mechanical measurements collected from the PED samples. Error bars represent a 95% confidence interval ( $n=3$ ) and the dashed lines indicate ROM predictions. The star markers indicate statistically significant measurements ( $p < 0.05$ ).

$\sigma_{YS}$  and  $\sigma_{UTS}$  were in reasonable agreement with rule of mixtures (ROM) predictions of 691 and 1090 MPa, respectively. While elongation was somewhat improved in the ML sample, it fell short of ROM behavior. Tensile failure is a complicated process which is driven by the evolution of the stress-state from a global-uniaxial to a localized-multiaxial condition, and therefore a simple ROM behavior for elongation of the ML cannot be assumed. A detailed investigation of the development of strain localization and plastic interaction between constituents is required in order to understand deformation behavior in the ML architecture.

### 3.2. Uniform deformation hardening behavior and strain localization during necking

In order to understand uniform deformation behavior during tensile loading, the hardening response of the PED samples was examined. As shown in Fig. 7, the tangent moduli of the ML and NC samples decayed in a linear manner, conforming to Stage III work hardening, whereas the CG sample exhibited both linear Stage III and near-asymptotic Stage IV behavior [34]. The tangent modulus ( $\theta$ ) is presented here as the ratio of differential true stress ( $\sigma_t$ ) and true strain ( $\epsilon_t$ ) and the data in the figure is plotted until the point of peak load in each sample respectively. The absence of Stage IV in the ML tensile data suggested that NC layer work hardening mechanisms were dominant during uniform elongation and that contributions from the CG layer were negligible prior to necking. Considering the microstructure architecture of the ML and the weakest-link nature of tensile loading, this behavior was expected and is a consequence of the uniaxial stress-state prior to neck formation.

The non-uniform deformation behavior during necking was captured using DIC analysis. An image of a representative tensile coupon speckled for DIC analysis is presented in Fig. 8a and b presents line-scans of the strain profile along the normalized gauge length for each of the PED samples. The relative positions of the strain stages in each of the line-scans are indicated in the

**Table 1**

A summary of the mechanical measurements extracted from tensile testing of the PED samples.

PED sample	$\sigma_{YS}$ (MPa)	$\sigma_{UTS}$ (MPa)	$\epsilon_u$	$\epsilon_{nu}$	$R_a$
CG	$365 \pm 48$	$557 \pm 11$	$0.113 \pm 0.007$	$0.049 \pm 0.009$	$12.2 \pm 1.1$
ML	$664 \pm 15$	$1112 \pm 24$	$0.042 \pm 0.003$	$0.027 \pm 0.015$	$2.0 \pm 0.2$
NC	$1017 \pm 30$	$1622 \pm 39$	$0.037 \pm 0.004$	$0.020 \pm 0.006$	$1.5 \pm 0.2$

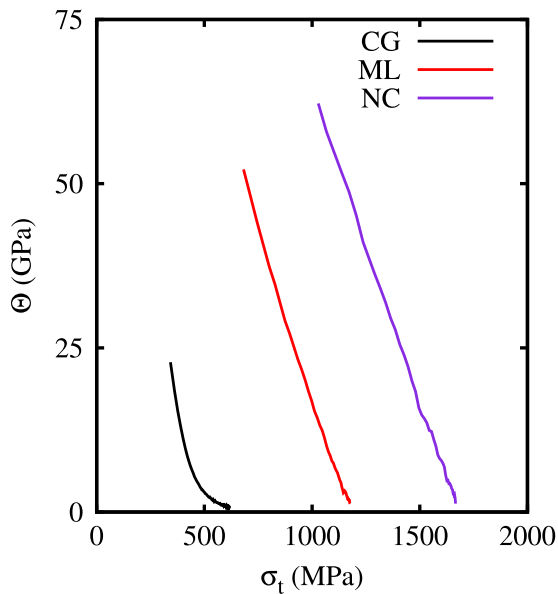


**Fig. 7.** Hardening data for the PED samples up until the peak load. All samples exhibited a linear decay in the tangent modulus, which was consistent with Stage III hardening. The CG sample also showed asymptotic Stage IV hardening. This behavior was absent in the ML sample, which indicated that the CG layer did not contribute significantly to deformation behavior before necking.

stress–strain curves of Fig. 4. The selected line-scans present the strain localization during the following deformation stages: post-yield uniform elongation; at peak load; after strain localization within tensile the neck; and immediately prior to coupon failure. In general, the progression of deformation in the PED samples was consistent. In each of the DIC tensile tests, the coupon failed within the gauge dimension of the sample. As anticipated from tensile data, each sample experienced a period of uniform elongation which transitioned to high strain localization just prior to failure. In the CG reference, fracture proceeded through strain development within a local neck. At strain stage 2, there were several local maximums along the gauge length. The largest of which developed into the localized neck. This behavior is well-known for materials with high strain hardening capabilities [35], where potential necks may stabilize during mechanical loading. In contrast to the CG reference, the NC and ML samples appeared to experience a mixed mode of deformation behavior, with diffuse and local necks evident in the strain maps. In order to examine the relative size of macroscale deformation features, a methodology that tracks changes in the strain profiles during loading was proposed. The size of the diffuse ( $L_{dn}$ ) and local necks ( $L_{ln}$ ) were quantified by considering the spatial and temporal derivatives of the DIC line-scans. Excluding the shoulder, the diffuse neck represented the length of the tensile coupon where the tangent of the strain profile deviated from zero (i.e.  $|dc/dx| > 0$ ). Similarly, the local neck was identified near the point of fracture when the temporal derivative of strain increased significantly from zero (i.e.  $dc/dt > 0$ ). The degree of strain localization ( $\epsilon_{ln}$ ) was then calculated as the difference from the peak strain to the baseline at the incidence of the local neck. The definition of these measurements is illustrated in Fig. 8c and the corresponding derivatives were calculated for each of the PED sample line-scans presented in Fig. 8b. The calculated quantities of  $L_{dn}$  and  $L_{ln}$  were normalized against  $W_0$  and these measurements, along with  $\epsilon_{ln}$ , are provided in Table 2. From this analysis, the CG sample possessed the highest degree of strain localization. Notably, the strain localization in the ML sample was much larger than the NC reference, indicating a significant contribution from the CG layers to deformation behavior within the tensile neck. It should be noted that a distinction

between the local and diffuse necks could not be established for the CG sample. The CG measurements are therefore considered as localized neck values.

In order to compare the local necks in the PED samples, DIC strain maps were collected just prior to fracture (Fig. 9). The colormap is normalized with respect to maximum engineering strain within each of the PED samples and the final dimensions of each tensile coupon are scaled to fit the image frame. As anticipated from tensile stress–strain data, the CG sample appeared to fail by conventional necking mechanisms. Conversely, strain localization in the ML and NC samples was confined to a band rotated  $55^\circ$  to the loading axis. Macroscopic shear banding at this angle is a commonly reported fracture mechanism in bulk nanocrystalline metals [36–38] and is a result in the collapse of dislocation storage capacity within nanoscale microstructures [17,18]. It is interesting to note that although the ML sample appeared to fail macroscopically by NC dominated shear banding, the extent of strain localization within the band was substantially higher than the NC reference, indicating a significant contribution to material plasticity from CG layers (Fig. 8b).

### 3.3. Multiscale deformation mechanism within the tensile neck

In order to gain insight into the interplay between fracture morphology and microscale plasticity within the tensile neck of the ML samples, SEM images captured perpendicular to the loading axis of the coupon are provided in Fig. 10. The low magnification images presented in Figs. 10a and b are mating fracture surfaces and examination of the images revealed a number of interesting features. As in DIC analysis of the planar dimensions, the fracture plane also appeared inclined at  $55^\circ$  to the loading axis through the coupon cross-section. The shear band is therefore inclined at compound angles of  $55^\circ$  to the loading axis in both the planar and cross-section views, forming a fracture plane which sectioned the waist of the tensile coupon along an oblique path (Fig. 10b). Consequently, although the fracture plane initiated at the thinnest cross-section, fracture did not propagate directly through the waist. This phenomenon was a factor responsible for the drastic reduction in  $R_a$  relative to the CG reference. It is interesting to note that in the cross-section view the fracture plane appeared to fall along planes oriented  $\pm 55^\circ$  to the loading axis. Conversely, observations from DIC testing showed a single fracture path in the planar view. This behavior was not observed in the NC sample (Fig. 5c) and was unique to the ML coupons. It is possible that the laminate layering of CG microstructure through the sample cross-section disrupted the formation of a singular shear band orientation, permitting a mixed fracture plane. On the microscopic scale, the flow of NC and CG layers into the multiaxial stress field of the localized neck is clearly visible in Fig. 10b. A higher magnification micrograph (Fig. 10c) images the interfacial boundary between layers in the tensile neck. The pronounced refinement and distortion of the CG layer microstructure near the ML interface was likely the result of interfacial dislocation activity which was caused by the multiaxial stress-state resulting from macroscopic strain localization in both the diffuse and local necks. From a macromechanical perspective, this deformation accommodation in the interfacial structures was believed to contribute to the comparatively increased tensile strain measured within the necking region of the ML (Fig. 8b).

As observed in reduction area measurements (Fig. 5c), the fracture surface shown in Fig. 10a is populated by a landscape of dimpled CG and NC features. In order to gain insight into the relative topography of these features, FIB milling was implemented to cut a trench within the fracture plane and image the cross-section of the dimpled features. Fig. 11a presents a low magnification SEM image which provides perspective for the higher magnification images. The

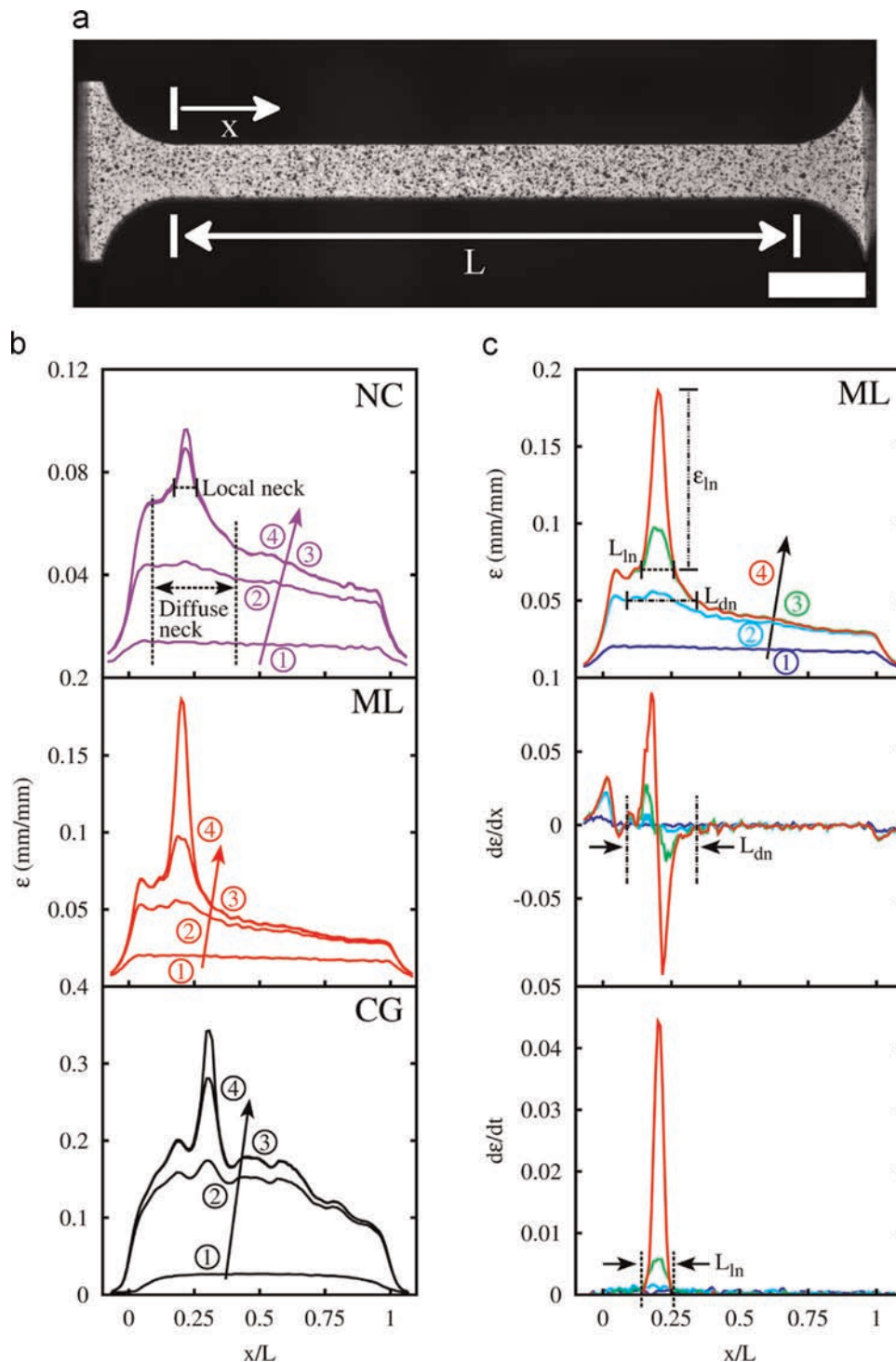


**Fig. 8.** (a) A photograph of a tensile coupon speckled for DIC measurements. The normalized length ( $x/L$ ) was defined as indicated in the image. (b) The strain profiles along the gauge length of the PED samples at various stages: (1) during uniform elongation; (2) at peak load; (3) at the initiation of localized necking; and (4) immediately prior to fracture. The relative positions of these stages are indicated on the stress–strain curves provided in Fig. 4. (c) Measurements of the diffuse ( $L_{dn}$ ) and local necks ( $L_{in}$ ) were defined by considering the spatial and temporal derivatives of the strain profiles in (a) for the ML sample. The strain localization in the local neck ( $\epsilon_{in}$ ) was defined as the peak strain subtracted from the baseline of the local neck length. The scale bar in (a) is 5 mm.

FIB was positioned such that the trench was aligned approximately parallel to the loading axis. The resulting milled surface is imaged in Fig. 11b. The axes provided in the figure may be referenced with respect to Fig. 11a. Despite the large deformation near the fracture surface, backscatter SEM imaging (Fig. 11c) of the trench cross-section revealed a faint channeling contrast in the underlying microstructure of the fracture surface. From these microstructure features, it can be seen that the large dimples correspond to failure in the CG

layer whereas the finer dimples represent fracture in the NC layer. Note that the bright layer visible in the image is a surface-conforming protective layer of tungsten which was deposited to prevent damage to the underlying material and also assisted in visualizing the topographical landscape of the fracture surface. Further examination of the trenched cross-section showed that the CG layers have a saw-toothed shape that protruded approximately 2–3  $\mu\text{m}$  above the fracture plane. The outline of these features was measured

**Table 2**  
The width-normalized lengths of the diffuse and local necks, and strain localization in the PED samples.

PED sample	$L_{dn}$	$L_{ln}$	$\epsilon_{ln}$
CG	–	$\approx 2W_0$	0.18
ML	$\approx 3W_0$	$\approx W_0$	0.11
NC	$\approx 3.5W_0$	$\approx W_0$	0.03

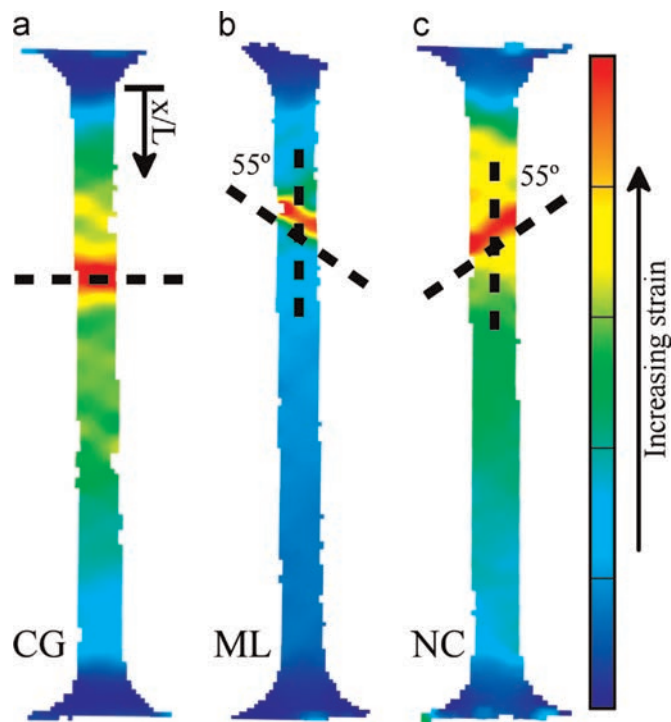


**Fig. 9.** The strain distribution across the (a) CG, (b) ML, and (c) NC tensile coupons immediately prior to fracture. Macroscopic shear banding at  $55^\circ$  from the loading axis was evident in the ML and NC samples. The colormapping represents a normalization of the maximum strains in each corresponding PED sample.

to be approximately  $45^\circ$  from the loading axis. Considering the  $\langle 100 \rangle$  texture measured in the EBSD data (Fig. 2), and the proximity of the observed CG layer fracture angle relative to the localized neck ( $55^\circ$  to the loading axis), this fracture orientation likely corresponds to activation of the  $\langle 110 \rangle / \{ 111 \}$  slip system, which has been previously reported as a possible deformation mechanism in NiFe MLs [23].

The deformation behavior of the NiCo ML is an inherently multiscale phenomenon in which the modulation of grain size on the microscale translates into the macroscopically observed fracture geometry. Fig. 12 presents a schematic representation of this multiscale deformation mechanism. In each test, tensile failure initiated from the surface of the coupon, which was consistent with observations in other mechanical studies of PED materials [39]. Due to the relatively low strain hardening capability of the NC layer, a macroscopic shear band formed, which developed into a localized neck. The change from a uniaxial to a multiaxial stress-state caused plastic interaction between the constituent layers and led to the formation of a shear band, which activated the  $\langle 110 \rangle / \{ 111 \}$  slip system in the CG layer and permitted the development of a significant neck. Continued elongation resulted in fracturing of both the NC and CG layers by microvoid coalescence. Macroscopically, the fracture plane initiated at the thinnest region of the loaded cross-section and propagated along the shear band. This behavior caused the waist of the tensile coupon to be cut along an oblique angle oriented at  $55^\circ$  from the loading axis along

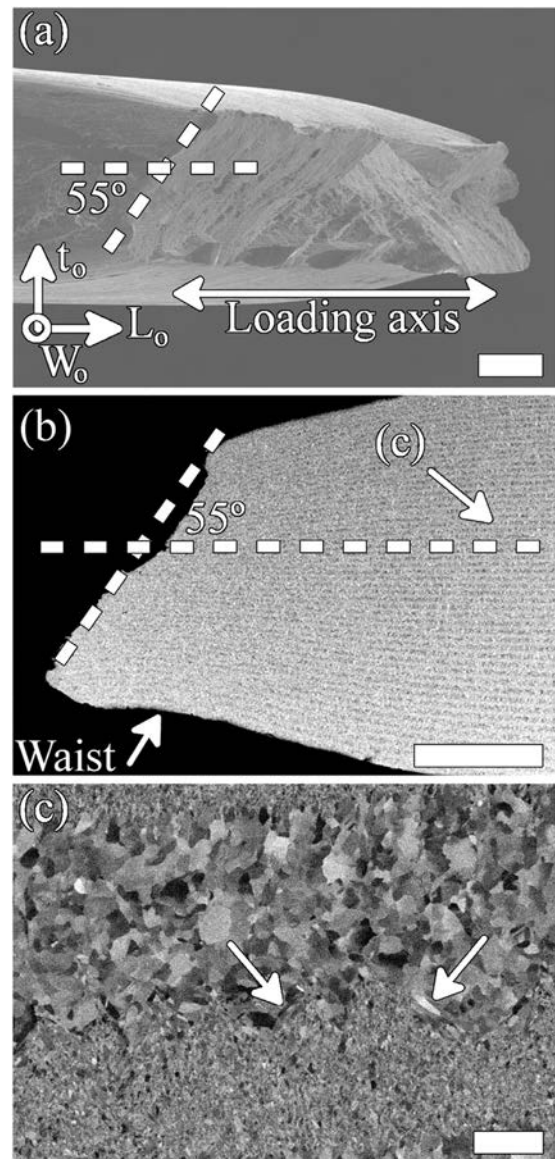


**Fig. 10.** (a) A low magnification SEM image of the fractured ML sample. The sample appears to have fractured through a shear band oriented at  $\pm 55^\circ$  to the loading axis. The orientation of the nominal tensile coupon dimensions relative to the image plane is provided. (b) An SEM image of the mating fracture surface to (a) after polishing. The flow of CG and NC layers into the neck is evident. The fracture path initiated at the thinnest region of the coupon waist and propagated along an oblique path, following the observed shear band. (c) A high magnification SEM micrograph of the CG and NC layers within the diffuse neck. Arrows highlight distortion in the CG microstructure along the interface between layers, suggesting dislocation activity that contributed to the improved necking stability in the ML. The scale bars are 200 in (a) and (b), and  $2 \mu\text{m}$  in (c).

the width and thickness of the sample. In comparison to the CG sample, the oblique orientation of the fracture path relative to the loading axis was also likely the cause of the drastically reduced  $R_f$ . The relatively small area reduction due to uniform elongation is not represented in the schematic. On the microscopic scale, the dimpled fracture surface was populated by periodic saw-toothed protrusions which revealed the topographical landscape of the CG layer. It is expected that the orientation of CG protrusions in the fracture surface is highly texture dependent. A more randomized texture may lead to a less uniform saw-toothed fracture feature, but is not expected to significantly alter the interacting deformation mechanisms observed in the ML architecture.

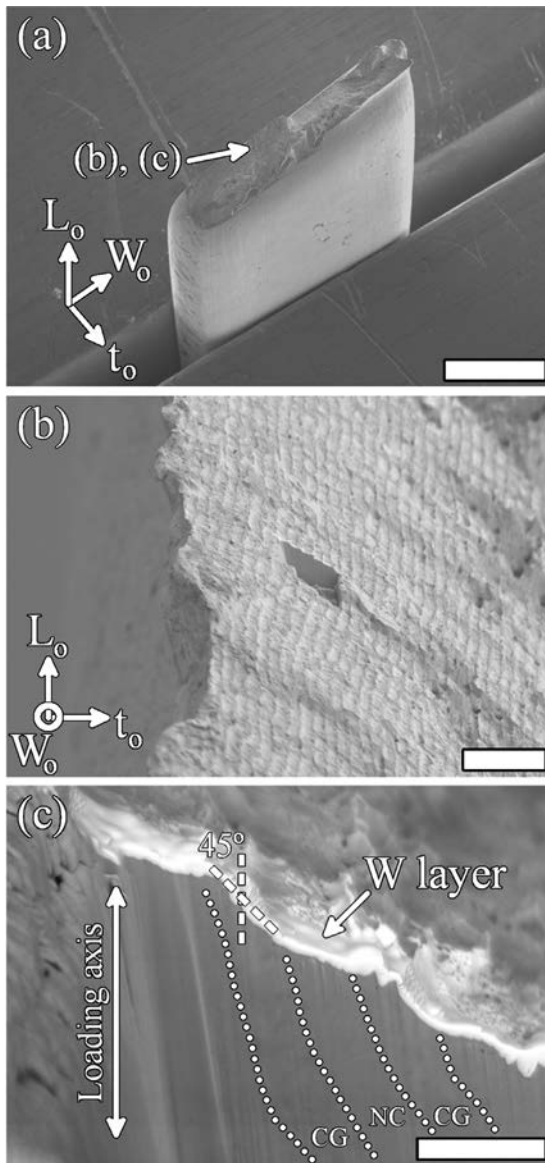


**Fig. 11.** (a) An SEM micrograph of the ML fracture surface taken from a perspective orientation. (b) An image of the trench which was cut using FIB milling. The trench is aligned approximately to the loading axis of the tensile coupon. The orientation of the nominal tensile coupon dimensions relative to the image plane is provided in (a) and (b). (c) A backscatter SEM image of a trench milled into the fracture surface. The protruding structures appear to have a saw-tooth geometry which were inclined at approximately  $45^\circ$  to the loading axis. The scale bars are 1 mm (a), 50  $\mu\text{m}$  (b), and 5  $\mu\text{m}$  (c).

#### 4. Conclusions

The deformation behavior of a pulse electrodeposited NiCo multilayer with an alternating grain size distribution was studied. Uniaxial testing showed a rule of mixtures yield and tensile strength in the ML relative to CG and NC references. Digital image correlation analysis and examination of the ML fracture surface offered important insight into the micro- and macroscale deformation mechanisms leading to ultimate material failure. Based on these observations, a multiscale mechanism was proposed to describe the deformation behavior in MLs with modulated hard-soft NC and CG layers. Fracture was preceded by the development of a diffuse and local neck within the ML sample. Inside the local neck, a shear band was observed to form. The shear band was oriented at  $55^\circ$  to the loading axis along both the coupon width and the thickness. Upon the formation of a shear band, the

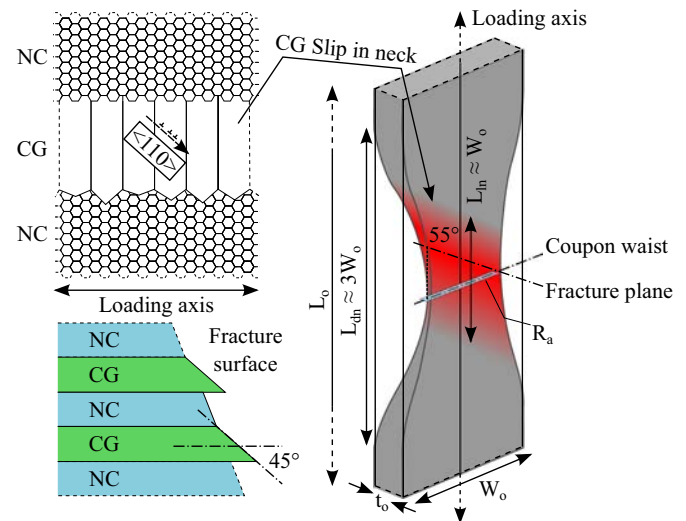


**Fig. 12.** The proposed multiscale deformation mechanism for MLs with modulated hard-soft NC and CG layers. Micro- and macroscale deformation phenomena are illustrated schematically during necking and upon ultimate fracture of the ML. Material flowed from the diffuse into the localized neck where fracture initiated along the shear band at the thinnest region. The fracture plane cut across the coupon waist at an oblique angle of  $55^\circ$  through the sample width and thickness. The projection of this fracture plane is the measurement  $R_a$ . On the microscale, the activation of the  $\langle 110 \rangle / \{111\}$  slip system in the CG layer manifested into the saw-toothed protrusions observed in SEM micrographs of the ML fracture surface.

resulting multiaxial stress state induced significant deformation in the CG layer, improving the neck stability in the ML. Further elongation of the sample resulted in ultimate failure with fracture initiating at the thinnest point of the neck cross-section and propagating along the shear band, which sectioned the coupon waist at an oblique angle relative to the loading axis. High magnification SEM micrographs indicated dislocation activity across ML interfaces, leading to significant material plasticity and improved non-uniform ductility within the sample neck. Furthermore, failure of the CG layers yielded periodic topographical features which protruded from the fracture surface. The saw-toothed topography was created by activation of the  $\langle 110 \rangle / \{111\}$  slip system in the ML, which was a consequence of the texture of the CG layer as well as the orientation of a shear band during tensile loading.

#### Acknowledgments

The authors would like to acknowledge the assistance of Sal Boccia of the Materials Science and Engineering department at the University of Toronto as well as Patrick Woo of Hitachi High Technologies Canada Inc. for their helpful comments and guidance in regard to SEM imaging. Additionally, the authors are grateful for the help of Karim Danaei in collecting XRD measurements, Ante Lausic for assistance with DIC image collection, and Balaji Venkatesh for advice on EBSD pattern collection. C.V.S. and G.D.H. acknowledge funding from the Natural Science and Engineering Council of Canada (NSERC) and the University of Toronto. M.D. would like to acknowledge funding from the NSERC Postgraduate Scholarships Program. Financial support from the Office of Naval Research under Grant N00014-10-C-0371 with Dr. Lawrence Kabacoff as Program Manager is gratefully acknowledged.

#### References

- [1] J.S. Koehler, Attempt to design a strong solid, *Phys. Rev. B* 2 (2) (1970) 547–551.
- [2] P. Anderson, C. Li, Hall–Petch relations for multilayered materials, *Nanostruct.*

- Mater. 5 (3) (1995) 349–362, [http://dx.doi.org/10.1016/0965-9773\(95\)00250-1](http://dx.doi.org/10.1016/0965-9773(95)00250-1).
- [3] L. Fang, L.H. Friedman, Analytic treatment of metallic multilayer strength at all length scales: influence of dislocation sources, *Acta Mater.* 55 (5) (2007) 1505–1514, <http://dx.doi.org/10.1016/j.actamat.2006.10.012>.
- [4] D. Tench, J. White, Enhanced tensile strength for electrodeposited nickel–copper multilayer composites, *Metall. Trans. A* 15 (A) (1984) 2039–2040, <http://dx.doi.org/10.1007/BF02663027>.
- [5] R.G. Hoagland, T.E. Mitchell, J.P. Hirth, H. Kung, On the strengthening effects of interfaces in multilayer fcc metallic composites, *Philos. Mag. A* 82 (4) (2002) 643–664, <http://dx.doi.org/10.1080/01418610208243194>.
- [6] R.G. Hoagland, R.J. Kurtz, C.H. Henager, Slip resistance of interfaces and the strength of metallic multilayer composites, *Scripta Mater.* 50 (6) (2004) 775–779, <http://dx.doi.org/10.1016/j.scriptamat.2003.11.059>.
- [7] D. Bhattacharyya, N. Mara, P. Dickerson, R. Hoagland, A. Misra, Transmission electron microscopy study of the deformation behavior of Cu/Nb and Cu/Ni nanoscale multilayers during nanoindentation, *J. Mater. Res.* 24 (03) (2009) 1291–1302, <http://dx.doi.org/10.1557/jmr.2009.0147>.
- [8] A. Misra, M.J. Demkowicz, J. Wang, R.G. Hoagland, The multiscale modeling of plastic deformation in metallic nanolayered composites, *JOM* 60 (4) (2008) 39–42, <http://dx.doi.org/10.1007/s11837-008-0047-6>.
- [9] J. Wang, A. Misra, An overview of interface-dominated deformation mechanisms in metallic multilayers, *Curr. Opin. Solid State Mater. Sci.* 15 (1) (2011) 20–28, <http://dx.doi.org/10.1016/j.cossms.2010.09.002>.
- [10] J. Wang, R.G. Hoagland, J.P. Hirth, A. Misra, Atomistic modeling of the interaction of glide dislocations with “weak” interfaces, *Acta Mater.* 56 (19) (2008) 5685–5693, <http://dx.doi.org/10.1016/j.actamat.2008.07.041>.
- [11] H. Huang, F. Spaepen, Tensile testing of free-standing Cu, Ag and Al thin films and Ag/Cu multilayers, *Acta Mater.* 48 (12) (2000) 3261–3269, [http://dx.doi.org/10.1016/S1359-6454\(00\)00128-2](http://dx.doi.org/10.1016/S1359-6454(00)00128-2).
- [12] J.Y. Zhang, G. Liu, X. Zhang, G.J. Zhang, J. Sun, E. Ma, A maximum in ductility and fracture toughness in nanostructured Cu/Cr multilayer films, *Scr. Mater.* 62 (6) (2010) 333–336, <http://dx.doi.org/10.1016/j.scriptamat.2009.10.030>.
- [13] Y.P. Li, G.P. Zhang, On plasticity and fracture of nanostructured Cu/X (X = Au, Cr) multilayers: the effects of length scale and interface/boundary, *Acta Mater.* 58 (11) (2010) 3877–3887, <http://dx.doi.org/10.1016/j.actamat.2010.03.042>.
- [14] N.A. Mara, D. Bhattacharyya, P. Dickerson, R.G. Hoagland, A. Misra, Deformability of ultrahigh strength 5 nm Cu/Nb nanolayered composites, *Appl. Phys. Lett.* 92 (23) (2008) 231901, <http://dx.doi.org/10.1063/1.2938921>.
- [15] J. Weertman, Hall–Petch strengthening in nanocrystalline metals, *Mater. Sci. Eng.: A* 166 (1–2) (1993) 161–167, [http://dx.doi.org/10.1016/0921-5093\(93\)90319-A](http://dx.doi.org/10.1016/0921-5093(93)90319-A).
- [16] A. Robertson, U. Erb, G. Palumbo, Practical applications for electrodeposited nanocrystalline materials, *Nanostruct. Mater.* 12 (5) (1999) 1035–1040, [http://dx.doi.org/10.1016/S0965-9773\(99\)00294-9](http://dx.doi.org/10.1016/S0965-9773(99)00294-9).
- [17] D. Jia, K.T. Ramesh, E. Ma, Failure mode and dynamic behavior of nanophase iron under compression, *Scripta Mater.* 42 (1) (1999) 73–78, [http://dx.doi.org/10.1016/S1359-6462\(99\)00312-7](http://dx.doi.org/10.1016/S1359-6462(99)00312-7).
- [18] D. Jia, K.T. Ramesh, E. Ma, Effects of nanocrystalline and ultrafine grain sizes on constitutive behavior and shear bands in iron, *Acta Mater.* 51 (12) (2003) 3495–3509, [http://dx.doi.org/10.1016/S1359-6454\(03\)00169-1](http://dx.doi.org/10.1016/S1359-6454(03)00169-1).
- [19] E. Ma, Instabilities and ductility of nanocrystalline and ultrafine-grained metals, *Scripta Mater.* 49 (7) (2003) 663–668, [http://dx.doi.org/10.1016/S1359-6462\(03\)00396-8](http://dx.doi.org/10.1016/S1359-6462(03)00396-8).
- [20] V.L. Tellkamp, E.J. Lavernia, A. Melmed, Mechanical behavior and microstructure of a thermally stable bulk nanostructured Al alloy, *Metall. Mater. Trans. A* 32 (9) (2001) 2335–2343, <http://dx.doi.org/10.1007/s11661-001-0207-6>.
- [21] B. Raesinia, C.W. Sinclair, W.J. Poole, C.N. Tomé, On the impact of grain size distribution on the plastic behaviour of polycrystalline metals, *Model. Simul. Mater. Sci. Eng.* 16 (2) (2008) 025001, <http://dx.doi.org/10.1088/0965-0393/16/2/025001>.
- [22] Y. Wang, M. Chen, F. Zhou, E. Ma, High tensile ductility in a nanostructured metal, *Nature* 419 (6910) (2002) 912–915, <http://dx.doi.org/10.1038/nature01133>.
- [23] L. Kurmanaeva, H. Bahmanpour, T. Holland, J. McCrea, J.H. Lee, J. Jian, H. Wang, E.J. Lavernia, A.K. Mukherjee, Room temperature mechanical behaviour of a Ni–Fe multilayered material with modulated grain size distribution, *Philos. Mag.* 94 (31) (2014) 3549–3559, <http://dx.doi.org/10.1080/14786435.2014.964346>.
- [24] P. Nash, Phase Diagram of Binary Nickel Alloys, ASM International, USA, 1991.
- [25] G.D. Hibbard, K.T. Aust, U. Erb, Thermal stability of electrodeposited nanocrystalline Ni–Co alloys, *Mater. Sci. Eng. A* 433 (1–2) (2006) 195–202, <http://dx.doi.org/10.1016/j.msea.2006.06.096>.
- [26] U. Erb, A. El-Sherik, Nanocrystalline Metals and Process of Producing the Same, 1994.
- [27] A. El-Sherik, U. Erb, Synthesis of bulk nanocrystalline nickel by pulsed, *J. Mater. Sci.* 30 (1995) 5743–5749.
- [28] U. Erb, Electrodeposited nanocrystals: synthesis, properties and industrial applications, *Nanostruct. Mater.* 6 (5–8) (1995) 533–538, [http://dx.doi.org/10.1016/0965-9773\(95\)00114-X](http://dx.doi.org/10.1016/0965-9773(95)00114-X).
- [29] C. Chan, J. McCrea, G. Palumbo, U. Erb, Microstructural and mechanical characterization of multilayered iron electrodeposits, *Adv. Mater. Res.* 409 (2011) 474–479, <http://dx.doi.org/10.4028/www.scientific.net/AMR.409.474>.
- [30] S.H. Kim, H.J. Sohn, Y.C. Joo, Y.W. Kim, T.H. Yim, H.Y. Lee, T. Kang, Effect of saccharin addition on the microstructure of electrodeposited Fe–36 wt.% Ni alloy, *Surf. Coat. Technol.* 199 (1) (2005) 43–48, <http://dx.doi.org/10.1016/j.surfcoat.2004.11.035>.
- [31] H.E. Swanson, E. Tatge, Standard X-ray diffraction powder patterns, *Natl. Bur. Stand. Circ.* 539 (1) (1953) 13–15.
- [32] A. Ragab, S. Bayoumi, *Engineering Solid Mechanics: Fundamentals and Applications*, CRC Press, Boca Raton, FL, U.S.A., 1999.
- [33] W.C. Unwin, Tensile tests of mild steel: and the relation of elongation to the size of the test-bar, *Min. Proc.* 155 (1904) 170–233, <http://dx.doi.org/10.1680/imotp.1904.17921>.
- [34] U.F. Kocks, H. Mecking, Physics and phenomenology of strain hardening: the FCC case, *Prog. Mater. Sci.* 48 (3) (2003) 171–273, [http://dx.doi.org/10.1016/S0079-6425\(02\)00003-8](http://dx.doi.org/10.1016/S0079-6425(02)00003-8).
- [35] A.K. Ghosh, Strain localization in the diffuse neck in sheet metal, *Metall. Trans.* 5 (7) (1974) 1607–1616, <http://dx.doi.org/10.1007/BF02646332>.
- [36] S. Cheng, E. Ma, Y.M. Wang, L.J. Kecskes, K.M. Youssef, C.C. Koch, U. P. Trociewitz, K. Han, Tensile properties of in situ consolidated nanocrystalline Cu, *Acta Mater.* 53 (5) (2005) 1521–1533, <http://dx.doi.org/10.1016/j.actamat.2004.12.005>.
- [37] F. Dalla Torre, H. Van Swygenhoven, M. Victoria, Nanocrystalline electrodeposited Ni: microstructure and tensile properties, *Acta Mater.* 50 (15) (2002) 3957–3970, [http://dx.doi.org/10.1016/S1359-6454\(02\)00198-2](http://dx.doi.org/10.1016/S1359-6454(02)00198-2).
- [38] T. Chan, Y. Zhou, I. Brooks, G. Palumbo, U. Erb, Localized strain and heat generation during plastic deformation in nanocrystalline Ni and Ni–Fe, *J. Mater. Sci.* 49 (10) (2014) 3847–3859, <http://dx.doi.org/10.1007/s10853-014-8099-1>.
- [39] I. Brooks, G. Palumbo, G.D. Hibbard, Z. Wang, U. Erb, On the intrinsic ductility of electrodeposited nanocrystalline metals, *J. Mater. Sci.* 46 (24) (2011) 7713–7724, <http://dx.doi.org/10.1007/s10853-011-5751-x>.